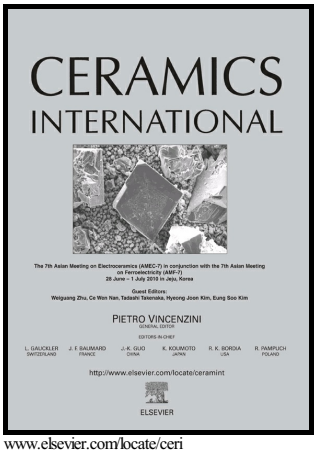

www.elsevier.com/locate/ceri

Microstructural and high-temperature impedance spectroscopy study of $Ba_6MNb_9O_{30}$ (M=Ga, Sc, In) relaxor dielectric ceramics with tetragonal tungsten bronze structure

Andrei. Rotaru, Finlay D. Morrison

PII: S0272-8842(16)30505-3
DOI: http://dx.doi.org/10.1016/j.ceramint.2016.04.102
Reference: CERI12720

To appear in: *Ceramics International*

Received date: 18 February 2016
Revised date: 18 April 2016
Accepted date: 19 April 2016

Cite this article as: Andrei. Rotaru and Finlay D. Morrison, Microstructural and high-temperature impedance spectroscopy study of $Ba_6MNb_9O_{30}$ (M=Ga, Sc In) relaxor dielectric ceramics with tetragonal tungsten bronze structure *Ceramics International,* http://dx.doi.org/10.1016/j.ceramint.2016.04.102

Microstructural and high-temperature impedance spectroscopy study of $Ba_6MNb_9O_{30}$ (M = Ga, Sc, In) relaxor dielectric ceramics with tetragonal tungsten bronze structure

Andrei Rotaru[1,2,*] and Finlay D. Morrison[2]

[1]*INFLPR – National Institute for Laser, Plasma and Radiation Physics, Laser Department, Bvd. Atomistilor, Nr. 409, 077125, Măgurele (Ilfov), Bucharest, Romania*

[2]*EaStCHEM Research School of Chemistry, University of St Andrews, North Haugh, KY16 9ST, St Andrews, Fife, Scotland, United Kingdom*

Abstract

This work reports on the microstructural and high-temperature impedance spectroscopy study of a family of dielectric ceramics $Ba_6MNb_9O_{30}$ (M= Ga, Sc, In) of tetragonal tungsten bronze (TTB) structure with relaxor properties. For $Ba_6GaNb_9O_{30}$ and $Ba_6InNb_9O_{30}$ pellets, the SEM images have revealed good, dense internal microstructures, with well-bonded grains and only discrete porosity; in contrast $Ba_6ScNb_9O_{30}$ pellets had a poorer microstructure, with many small and poorly-bonded grains gathered in agglomerates, resulting in significant continuous porosity and poorly defined grain boundary regions. The electroactive regions were characterised by the bulk and grain boundaries capacitances and resistances, while their contribution to the electrical conduction process was estimated by determining activation energies from the temperature (Arrhenius) dependence of both electric conductivities and time constants. For Ga and In analogues the electronic conductivity are dominated by the bulk response, while for Sc analogue, the poorly defined grain boundaries give a bulk-like response, mixing with the main bulk contribution.

Keywords: electrical conduction, grain boundary, high-temperature impedance spectroscopy, microstructure, relaxors, tetragonal tungsten bronzes.

*Corresponding author: andrei.rotaru@inflpr.ro

Telephone: +40745379205

1. Introduction

Within ceramic materials, a very interesting and important class is represented by electroceramics, which have useful electrical, optical and magnetic properties. Generally, electroceramics are advanced materials that are used in high technology applications. Their properties depend on the complex interplay of structural, processing and compositional variables. Even simple single-phase ceramic materials (not composite materials) have complex behaviour, of which usually the bulk (intrinsic) properties of the crystal are those of interest; therefore, dense ceramics – free from extrinsic effects (*e.g.* grain boundary, surface and electrode interfaces, dopant segregation, etc.) – are desired. They are used for various applications, as insulators, capacitors, temperature sensors and varistors, gas sensors, ionic electrolytes in fuel cell and rechargeable battery applications [1,2].

Insulators are chemical compounds that have the outer shell electrons locked in either strong covalent bonds or are restricted to close regions to an atomic nucleus (if the case of an ionic compound), and are unable to move through the structure in order to facilitate electrical conduction [1,2]. They are often referred as dielectrics, with the only mention that the term "insulator" is generally used to indicate *electrical obstruction* while the term "dielectric" is used to indicate the material *capacity to store energy*, *i.e.* to become polarised under an applied field. In dielectrics, the valence band is usually full; the next energy band is separated by a large forbidden band gap. As the forbidden band gap is larger, fewer electrons from the valence band have enough thermal energy to pass into the conduction band, and thus such materials become very good insulators. Solid dielectrics are definitely the most used dielectrics in electrical engineering, generally as: *a)* electrical insulating materials for coating or wrapping wires and cables that carry electric current (most plastics, electrical insulation paper, porcelain and glass) or *b)* as dielectric components in electronic devices (ceramics), such as rectifiers, transducers and amplifiers [3]. The required properties for a "good dielectric" are: high dielectric constant, low dielectric loss, thermal stability, tuneable temperature coefficients, high quality factors at many frequencies, high intrinsic breakdown for pulse power applications and resistance to interference from electromagnetic fields [4].

Polar dielectrics such as piezoelectrics or ferroelectrics are useful in electronic devices, as capacitors or resonators, mainly to their high permittivities [5]; with the demand for increasing the power processing of computers, the market was flooded with various multi-layer ceramic capacitors that led to a greater appreciation of the research concerning the relationship between chemical composition, structure and electrical properties of new dielectric materials [6-9]. Relaxor ferroelectric phenomenon was observed in ceramics

materials for nearly four decades [9-11]; for example, PMN-PT is a typical relaxor ferroelectric, with large piezoelectric effect and optical anisotropy [11].

More recently, besides the perovskite-based (ABO_3) materials, the tetragonal tungsten bronze (TTB) class of materials – Figure 1 – which is related to perovskites [12], has begun to garner renewed interest in the research community [12-15]. The very versatile TTB structure: $(A1)_2(A2)_4(C)_4(B1)_2(B2)_8O_{30}$ allows for the inclusion of particular metals into the five different TTB sites [16] and offers the possibility of adjusting both electric and magnetic behaviour [17,18]. The TTB structure has a repetitive perovskite unit in the middle (A1), while the additional corner-sharing BO_6 octahedra create another two types of channels in the structure: the A2-site and the C-site. The A1 sites are 12-coordinated and defined by 8 octahedra, the four larger A2 sites are 15-coordinated and defined by 10 octahedra, while the four trigonal C-sites are 9-coordinated and defined by 6 octahedra; moreover, the BO_6 octahedra are non-equivalent (two B1 sites and eight B2 sites) – Figure 1. This rich diversity of elements which can be incorporated into the TTB structure allows for compositional tuning that has been exploited for development of new phases [13,19] ranging from ferroelectrics [20-22] to microwave dielectrics [23,24] and to ionic conductors [25].

Figure 1 Polyhedral representation of the tetragonal tungsten bronze (TTB) aristotype structure viewed down the c-axis.

During the last few years, the research dedicated to novel TTB ferroelectric and ferroelectric-related materials resurrected [15-22,26-31], with the $Ba_6FeNb_9O_{30}$ (BFNO) [32-35] as starting point. Earlier data reported that BFNO is ferroelectric with T_C values either in the range 133-138 K [36] or 570-583 K [37,38], however being not electrically homogeneous [29] and with oxygen vacancy gradients due to the variable oxidation state of Fe (Fe^{3+}/Fe^{2+}); both low temperature dielectric spectroscopy and high temperature impedance spectroscopy measurements indicated more electroactive regions than anticipated [16].

A family of relaxor TTBs of composition $Ba_6M^{3+}Nb_9O_{30}$, where the trivalent species do not have variable oxidation states (*e.g.* Ga^{3+}, Sc^{3+}, In^{3+}) was chosen in order to avoid these additional complications during the study of this type of materials and reported by Arnold & Morrison [16]. Prior to this study, identical powders and pellets of these three Ga, Sc and In analogues of $Ba_6MNb_9O_{30}$ ceramic materials, prepared under the same conditions, were investigated by temperature-dependent powder neutron diffraction (TDPND) and by dielectric spectroscopy (DS); the confirmation of the phase formation and the crystallographic

identification, but also the relaxor dielectric properties of these dense ceramic materials were already reported [39]. The analysis of dielectric data showed a systematic (almost linear) increase in the dipolar stability of these materials with increasing M^{3+} cation size. Characteristic temperature parameters for each compound were extracted from both dielectric and crystallographic data as a function of temperature: the Vogel-Fulcher dipole freezing temperature, T_{VF}; T_{UDR} corresponding to absolute flattening of the dielectric loss peak in the frequency domain; and $T_{c/a}$ corresponding to the maximum crystallographic tetragonal strain. These temperature parameters were essentially coincidental and describe the slowing of dipolar response on cooling and the eventual "locking" of the B-cation displacements along the *c*-axis, (*i.e.* dipole freezing) [39]. The dynamics of dielectric relaxation of dipoles was extensively investigated by fitting the dielectric permittivity data to the Vogel-Fulcher (VF) model in order to monitor the reproducibility and validity of the physical results. We have shown that Vogel-Fulcher fits are very sensitive. Constraining some of the fundamental relaxation parameters to physically sensible values or varying the fitting range itself, results in a large range of values associated with the dielectric relaxation processes; restriction of the frequency domain due to experimental noise or instrumentation limits also has a dramatic influence on the values obtained [40].

Recently, resonance ultrasound spectroscopy (RUS) investigation of our Ga-analogue revealed that the main relaxor behaviour is accompanied by both elastic and anelastic relaxations [41]. In addition to an understanding of the chemical bonding, crystal structure and macroscopic dielectric properties, it is very important to understand the ceramic microstructure [42] and to identify and characterise the electrical behaviour of micro-regions [1,43-45] in order to fully characterize these ceramic materials. For adjusting technological conditions to prepare electroceramic materials, microstructure (grain homogeneity, grain morphology – shape and size, grain orientation, grain boundaries) must be determined and understood. Moreover, imperfections and defects affect all sorts of properties, by changing electrical behaviour, creating dislocations and finally producing mechanical failure. In this paper, the ceramic microstructure for three compositions, $Ba_6MNb_9O_{30}$ (M=Ga, Sc, In) was investigated in order to identify the electroactive regions present within these materials, and identify their influence on the macroscopic dielectric response. The capacitances and resistivities for both bulk and grain boundaries were estimated using combined impedance and modulus spectroscopy. The electric conductivities and the time constants were determined for both bulk and grain boundary regions and their contribution to the overall electrical conduction processes were investigated.

2. Experimental

2.1. Materials

Three ceramic compositions: $Ba_6MNb_9O_{30}$ (M=Ga, Sc, In) [16] were synthesised by standard solid-state techniques. Stoichiometric ratios of dried $BaCO_3$, Nb_2O_5, Ga_2O_3, In_2O_3, (all Aldrich, 99+%) and Sc_2O_3 (Stanford Materials Corporation, 99.999%) were ball milled in ethanol until homogenized (5 mins at 400 rpm, using a Fritsch Pulverisette 7 system with agate mortar and balls). Powders were placed on platinum foil in alumina boats inside a muffle furnace at 600 °C (static air atmosphere) and fired initially to 1000 °C, left to decarbonate for 1 hour, and further fired for 12 hours at 1250 °C (heating rates: 10 $K \cdot min^{-1}$). After quenched to room temperature, they were reground and heated at 1250 °C for a further 12 hours in alumina boats inside the same muffle furnace. After re-milling under the same conditions powders were subsequently re-sintered for 6.5 hours each, in a tube furnace at the following temperatures: 1300 °C (for $Ba_6GaNb_9O_{30}$) and 1350 °C (for $Ba_6ScNb_9O_{30}$ and $Ba_6InNb_9O_{30}$ – Table 1.

Pellets of these three materials were prepared by uniaxial pressing the powders to 1-1.1 tonne in a 10 mm diameter stainless steel die, producing a pressure of around 125-140 MPa. The green bodies were sintered on platinum foil in alumina boats inside a tube furnace for 6.5 hours at the temperatures previously reported in Ref. 16, *i.e.*, 1300 °C for $Ba_6GaNb_9O_{30}$, and 1350 °C for $Ba_6ScNb_9O_{30}$ and for $Ba_6InNb_9O_{30}$; then cooled down to room temperature (heating and cooling rates used were of 10 $K \cdot min^{-1}$) [16]. The obtained cylindrical pellets had diameters typically between 9.6 and 9.9 mm; a precise description of the relative densities obtained after sintering, but also of the employed reaction temperatures, sintering temperatures and their corresponding times are presented in Table 1.

Table 1 Fabrication details of $Ba_6M^{3+}Nb_9O_{30}$ (M^{3+} = Ga^{3+}, Sc^{3+}, In^{3+}) ceramic powders and pellets, and relative densities of the resulting pellets used for electrical studies

2.2. Investigation techniques

In order to probe or distinguish between different regions within the ceramic, microstructural characterization techniques shall be used [44]. Electron microscopy techniques with incorporated analytical facilities have been widely used for determining structural and compositional variations but provide limited or no insight into differences in electrical behaviour. Although the electrical properties of materials are closely related to their physical microstructure, for the electrically active regions, the above mentioned technique is not appropriate, and techniques which combine microscopy and electrical probes are not easy to

handle [46]. Cathode-luminescence techniques [47] have been used to observe directly potential barriers at grain boundaries but again this is a complex technique which can be destructive to the sample. More commonly separation of grain boundary and bulk effects can be achieved by measuring electrical properties using techniques such as impedance spectroscopy [48].

For scanning electron microscopy (SEM) measurements, a JEOL JSM 5600 SEM machine with attached EDX system, providing 3.5 nm resolution and a magnification of 300,000× was utilised. The employed current was ranging between 10^{-9} and 10^{-12} A and the accelerating voltage from 0.5 to 30 kV. A copper cylinder, covered with carbon tape was secured onto an aluminium support. Small fragments of the ceramic pellets were placed on the carbon tape. The aluminium support was introduced into the JEOL JSM 5600 SEM machine and the scans were started only after vacuum was obtained in the chamber.

For the high-temperature impedance spectroscopy (HT-IS) measurements, both planar external surfaces of the dense ceramic pellets were polished with SiC paper, then covered with organic-platinum paste electrodes (C2011004D5, Gwent Electronic Materials Ltd, UK). Each pellet face was covered with electrode paste were dried at 80 °C and placed on platinum foil and cured at 900 °C for approximately 1 hour in order to obtain Pt electrodes (eliminate the organic parts) and sinter the electrode. The electroded samples were mounted in an impedance alumina jig, similar to the one designed by Bruce and West [49]; the impedance jig was placed in a horizontal tube furnace controlled to ± 1 ºC. The temperature was increased step by step and when samples had reaching the desired temperature, they were left to equilibrate for approximately 15-20 minutes before taking the measurement. A Hewlett Packard 4192A LF impedance analyser was used to collect data over a frequency range of *ca.* 5 Hz – 13 MHz, in the temperature range *r.t.*–900 K and under an applied ac voltage of 100 mV. Data analysis was carried out using commercial "ZView" software, version 2.9c [50]; both complex plane plots and spectroscopic plots of both impedance and modulus formalisms were utilised, as described in detail below.

3. Results and discussion

Under the present circumstances, an investigation of the pellet morphology for each analogue compound of the series ($Ba_6GaNb_9O_{30}$, $Ba_6ScNb_9O_{30}$ and $Ba_6InNb_9O_{30}$) was carried out in relation with the identification of the electroactive regions within the same materials by high-temperature impedance spectroscopy. Since the electric conductivities and also the time constants are following the Arrhenius law, it is therefore possible to better discriminate and

understand the contribution of the bulk and grain boundaries to the electrical conduction processes.

3.1. Microstructural analysis for $Ba_6MNb_9O_{30}$ (M = Ga, Sc, In) ceramics

In order to correlate to the electrical properties, SEM was used to determine the grain size and morphology and porosity. Surface features that are tilted toward or closer to the detector appear especially bright because electrons emitted from these regions have a great probability of reaching the detector. This fact can be used to distinguish raised features and depressions in the surface of the specimen [51].

All investigated pellets were white, with no evident colour gradient on the external or fractured surfaces; characteristic micrographs of the ceramic microstructures are given below. On the external surface of pellets, for all three analogues, similar features are present (Figure 2). The external microstructure is continuous and appears uniform; scratches on the surface are due to the polishing process (using SiC polishing paper).

Figure 2 SEM micrographs for the external surfaces of a $Ba_6InNb_9O_{30}$ pellet.

The SEM images of $Ba_6GaNb_9O_{30}$ pellet revealed a highly dense microstructure with well-bonded grains (as shown from the intragranular nature of the fracture), and with only a few isolated pores, Figures 3a, 3b and 3d. The high processing temperature (1300 °C), which is close to the melting temperature, means that the $Ba_6GaNb_9O_{30}$ pellets sintered well (ρ_r = 94.55%, see Table 1) and this is consistent with the SEM images. The parallelepiped/columnar nature of the grains can be observed on the interior surfaces of isolated pores (left lower corner in Figure 3c); the grain size appears to be fairly uniform and of the order of 5-10 μm.

Figure 3 SEM images of the fracture surface of a $Ba_6GaNb_9O_{30}$ pellet sintered at 1300 °C.

The SEM images of $Ba_6ScNb_9O_{30}$ pellet, Figure 4, revealed a poor microstructure by comparison, with poorly-bonded grains sizes ranging from 2 to 10 μm and significant continuous porosity, again consistent with the lower relative density of 88%, Table 1.

Figure 4 SEM images of the fracture surface of a $Ba_6ScNb_9O_{30}$ pellet obtained at 1350 °C.

The majority of grains are almost round in morphology and are bonded to each other with neck-like grain boundaries – Figures 4b and 4c. There are also apparently denser

agglomerates formed of 4-5 bigger grains (of ~ 3 μm x 3.5 μm each) or of 10-20 smaller grains (of ~ 2 μm x 2.5 μm each) – Figures 4a and 4b. The area of these agglomerates vary from 20 x 25 μm^2 to 30 x 35 μm^2 and are linked by some independent small grains with irregular shapes and dimensions – Figures 4b and 4c. These agglomerates, however do not account for a very significant volume fraction and the majority of the sample consists of the fairly small grains with poor continuity – Figure 4c. The low processing temperature of 1350 °C (compared to the melting temperature which is higher than 1400 °C) may be the cause for the poor microstructure.

SEM images of $Ba_6InNb_9O_{30}$ pellet reveal a dense microstructure, with big grains and no clusters – Figures 5a and 5b. Many grains have columnar aspect (of ~ 3 μm x 7 μm each), while others have a melt-like appearance; the grains are well bonded resulting in clearly defined grain boundaries.

Figure 5 SEM images of the fracture surface of a $Ba_6InNb_9O_{30}$ pellet obtained at 1350 °C.

There is some discrete porosity, Figures 5c and 5d, but the majority of the sample consists of a continuous matrix of course grained material. These results confirm the high relative density (ρ_r = 92.15%, see Table 1) and most likely is a result of the high processing temperature (1350 °C), which approaches the melting temperature.

In the series of these three compounds, the $Ba_6GaNb_9O_{30}$ and $Ba_6InNb_9O_{30}$ pellets have sintered very well because they were subjected to temperatures close to their melting ones (50 °C less than 1350 °C and 1400 °C, respectively); therefore it has resulted in robust and dense materials. The microstructure of the $Ba_6ScNb_9O_{30}$ pellet, which was sintered at 1350 °C, is not that good in comparison with that of the other two and this affects the electrical properties as discussed below.

3.2. High-temperature impedance spectroscopy for $Ba_6MNb_9O_{30}$ (M = Ga, Sc, In) ceramics

In order to describe the behaviour of different electroactive regions within these ceramics, high temperature impedance spectroscopy studies have been carried out. Such AC methods used over a wide range of frequencies have obvious advantages over the conventional DC resistance method [48,52], providing a better understanding of different regions or even electrically inhomogeneity in materials. In most of the cases, the impedance spectroscopy plots are composed of several overlapping semicircular arcs (Nquist plots) or of Debye-like peaks representing the contributions of various components to the overall resistance and

capacitance of the sample. Each region has a characteristic response, and in a first approximation it can be modelled using an equivalent circuit consisting of parallel resistor-capacitor (RC) electrical elements that are connected in series; the product of the two R and C components gives a characteristic electrical relaxation time (or time constant), τ – equation 1, which is unique to a region within a material [48,52].

$$\tau_i = R_i \cdot C_i \quad (1)$$

The microstructural results suggest that the pellets of all three analogue TTB ceramics ($Ba_6GaNb_9O_{30}$, $Ba_6ScNb_9O_{30}$ and $Ba_6InNb_9O_{30}$) might consist of bulk and grain boundary regions that would be represented by two RC elements, one associated with the bulk (intragranular) response and the another may be the grain boundary (or other thin layer effects) [32,53,54]. There are cases when other electroactive regions manifest in the electrical responses; they can be described as well by parallel RC elements placed in series with those used for the grain boundary and bulk regions. Such additional parasite regions usually are surface layers or non-ohmic pellet/electrode contacts [52].

RC elements were separated into independent *R* (resistance) and *C* (capacitance) values by using both impedance and electric modulus [44,55]. Each RC element gives rise to a semicircle in the complex impedance (*Z**: $Z^* = Z' - j \cdot Z''$) plot and to another one in the complex electric modulus (*M**: $M^* = M' + j \cdot M'' = j \cdot \omega \cdot C_0 \cdot Z^*$) plot – for example, the Nquist plot in Figure 6d. As well, it gives rise to a Debye-like peak in the spectroscopic plot of the imaginary impedance (*Z''*) *vs.* frequency (*i.e.* Figure 6a) and in the spectroscopic plot of the imaginary electric modulus (*M''*) *vs.* frequency (*i.e.* Figure 6b) – representation, on a logarithmic scale of frequencies [52].

For almost perfect semicircles, reasonably accurate values of *R* and *C* may be obtained from the intercepts in the complex plane plots of *Z** (*Z'' vs. Z'*) or *M** (*M'' vs. M'*). However, for these samples (Figures 6d, 7d and 8d), there is present only one semicircle in each of the complex plots *Z** or *M**, and those semicircles are highly asymmetric; therefore, fittings are more difficult and time-consuming, while evaluations less accurate. The *Z''* and *M''* values in the Debye peak are described by equations 2 and 3:

$$Z'' = R\left(\frac{\omega RC}{1+(\omega RC)^2}\right) \quad (2)$$

$$M'' = \frac{\varepsilon_0}{C}\left(\frac{\omega RC}{1+(\omega RC)^2}\right) \quad (3)$$

where ω is the angular frequency ($\omega = 2\pi f$, where f is the frequency in Hz) and ε_0 is the permittivity of free space (8.854×10^{-14} F·cm^{-1}).

Debye peaks in *Z"* spectra are dominated by RC elements with largest *R* values whereas the *M"* spectra are dominated by RC elements with smallest *C* values (typically the largest volume fraction and therefore the bulk response).

The angular frequency (ω_{max}) at the maxima of *Z** or *M** semicircles, and correspondingly at the Debye peak maxima for each RC element is given by equation 4:

$$\omega_{max} = 2\pi f_{max} = (RC)^{-1} = \tau^{-1} \quad (4)$$

where f_{max} is the frequency at the peak maximum, the product $R\cdot C$ is the time constant, τ, of the corresponding RC element. The time constant and the frequency at the peak maximum are intrinsic characteristics of each the RC element (hey are independent of geometry) [52].

For a Debye response (ideal), the magnitude of the imaginary data at the peak maxima (*Z"* and *M"*), where $\omega\cdot R\cdot C = \omega_{max}\cdot R\cdot C = 1$, are given by:

$$Z''_{max} = R/2 \quad (5)$$

$$M''_{max} = \varepsilon_0/(2C) \quad (6)$$

By using these expressions 4-6, *R* and *C* values can be determined from Z''_{max} and M''_{max}, respectively. The electric response may be assigned therefore to: bulk region, grain boundary region or electrode surface, from the magnitude of the *C* values [44].

As a first stage of data analysis, the number of electroactive regions were evaluated from the number of Debye-like peaks in the *Z"* and *M"* spectrum and which appear at distinct relaxation frequencies. Since at room temperature the peaks are not present in the measuring frequency range (roughly, 10-10^7 Hz), measurements at higher temperatures have been carried out. However, up to considerable high temperatures in the M" plot (638 K for $Ba_6GaNb_9O_{30}$, 758 K for $Ba_6ScNb_9O_{30}$, 738 K for $Ba_6InNb_9O_{30}$) only a tail is observed instead of the entire peak (with f_{max} < 10 Hz) or at least the peak maximum. In the *Z"* plot also, up to the same high temperatures as in the *M"* plot – and even higher for $Ba_6GaNb_9O_{30}$ (778 K), only a tail is observed instead of the entire peak (with f_{max} < 10 Hz) or at least the peak maximum.

Starting with the temperatures indicated above, isothermal impedance spectroscopy measurements have been systematically carried out at every 20 degrees, up to 863 K. In these

temperature ranges, the entire peak maximum is observed allowing estimation of *R* and *C* values using the methodology described above.

For the $Ba_6GaNb_9O_{30}$ analogue, high-temperature impedance spectroscopy data are presented in Figure 6. The impedance appears to show two poorly resolved (overlapping) responses as indicated by the asymmetric peak in the *Z" vs. freq*. plot (Figure 6a) and the broad asymmetric semicircle in the complex (*Z**) *Z" vs. Z'* plane plot (at 761 K and at 802 K, for example). Moreover, at lower temperatures (at 720 K for example), the curve of *Z** complex plot is not only asymmetric, but clearly shows two independent responses (Figure 6d, upper graphic). By contrast, the presented electric modulus, which is more sensitive to the bulk, exhibits a single response (narrow and almost ideal response) in the Debye peak (*M" vs. freq.* plot, Figure 6b). The complex plot *M** contains a single semicircle, but with a degree of asymmetry, particularly at low frequency (Figure 6d, lower graphic). The higher frequency response which dominates the modulus spectra was attributed to the bulk response and the lower frequency one which dominates the impedance was assigned to the grain boundary. In Figure 6c it can be easily observed that the grain boundary and bulk time constants are separated by less than 3 orders of magnitude of frequency and are therefore hard to resolve; however as they dominate the impedance and modulus, respectively, it should be possibly to distinguish their character to some degree.

High-temperature impedance spectroscopy data for the $Ba_6ScNb_9O_{30}$ analogue are presented in Figure 7. Again the impedance data appears to show two responses as indicated by the asymmetric peak in *Z" vs. freq.* plot (Figure 7a) and the asymmetric semicircle in the complex (*Z**) *Z" vs. Z'* graphic (asymmetry at low frequencies in all experiments carried out at different temperatures

Figure 6 Selective high-temperature impedance spectroscopy data for $Ba_6GaNb_9O_{30}$: spectroscopic plot of *Z"* (a), *M"* (b) and combined *Z"* and *M"* plot at 802 K (c); complex impedance (*Z**) and modulus (*M**) plots (d).

Figure 7 Selective high-temperature impedance spectroscopy data for $Ba_6ScNb_9O_{30}$: spectroscopic plot of *Z"* (a), *M"* (b) and combined *Z"* and *M"* plot at 824 K (c); complex impedance (*Z**) and modulus (*M**) plots (d).

The electric modulus, which is more sensitive to the bulk, exhibits a single, narrow and almost ideal response in the Debye peak (*M" vs. freq.* plot, Figure 7b), but only at high

temperatures; at lower temperatures (783 K or 803 K), it is not a perfect Debye peak, with more asymmetry than for the other two compounds with Ga or In. The complex plot *M** contains a single semicircle, which was again assigned to the bulk response, but with a degree of asymmetry, particularly at high frequencies (Figure 7d, lower graphic). In Figure 7c it can be easily observed that the "grain boundary" and bulk responses have similar time constants, resulting in overlapping peaks in the frequency domain. The similarity of the time constants results from the poor microstructure of the $Ba_6ScNb_9O_{30}$ pellet as described in the previous section and mainly as can be observed from Figure 4. The poorly defined and neck-like nature of the grain boundaries results in a much more "bulk-like" response for these regions [48]. An in-depth analysis of the influence of microstructure and thermal processing of $Ba_6ScNb_9O_{30}$ ceramics on the electrical properties will be carried out in a subsequent work.

Selected impedance data for $Ba_6InNb_9O_{30}$ are presented in Figure 8 and contains similar features to the other samples. The impedance appears to show two responses as indicated by the asymmetric peak in *Z" vs. freq.* plot (Figure 8a) and the broad asymmetric semicircle in the complex (*Z**) *Z" vs. Z'* graphic (at low frequencies). By contrast, the presented electric modulus, which dominated by the bulk, exhibits a single response (narrow and almost ideal response) in the Debye peak (*M" vs. freq.* plot, Figure 8b). The complex plot *M** contains a single semicircle, but with only a low degree of asymmetry, particularly at very high frequencies (Figure 8d, lower graphic). In Figure 8c it can be easily observed that the frequency range grain boundary and bulk responses again overlap again making absolute deconvolution of their associated *R* and *C* values difficult.

For each sample the bulk capacitance, C_b, and "grain boundary" resistance, R_{gb}, were approximated from the magnitude of M''_{max} and Z''_{max}, using equations (5) and (6), respectively; the corresponding bulk resistance, R_b, was determined from expression (4). For all three analogues, the capacitance of the bulk (C_b) decreases systematically with increasing temperature, while the resistance of the bulk (R_b) also decreases. All C_b values are in the range 3.3-1.5×10^{-11} F·cm^{-1}, characteristic of bulk values [44]. At 843-844 K, C_b increases from 1.556×10^{-11} F·cm^{-1} for the Ga analogue, to 2.067×10^{-11} F·cm^{-1} for the Sc analogue, and respectively to 2.62×10^{-11} F·cm^{-1} for the In analogue. For the "grain boundary" capacitances (C_{gb}), the values are only slightly higher than for the bulk ones, largely due to mixing with the bulk response. The Sc analogue in particular has a lower than expected grain boundary capacitance (C_{gb}=2.602×10^{-11} F·cm^{-1} at 843 K) with practically the same value as the bulk. This is consistent with the more bulk-like nature of the necks between the grains as

determined by SEM, Figure 4. Based on the capacitance values and similarities of time constant (τ) of the bulk and "grain boundary" responses it is not clear that the data determines a "grain boundary" response in the true sense.

Figure 8 Selective high-temperature impedance spectroscopy data for $Ba_6InNb_9O_{30}$: spectroscopic plot of *Z"* (a), *M"* (b) and combined *Z"* and *M"* plot at 843 K (c); complex impedance (*Z**) and modulus (*M**) plots (d).

The high-temperature impedance spectroscopy data have revealed broadly similar behaviour of the three compounds; they are electrical insulators, with only moderate levels of conductivity at temperatures >350 °C.

3.3. Electrical conduction processes in $Ba_6MNb_9O_{30}$ (M = Ga, Sc, In) ceramics

The electrical conductivity, σ, of both bulk (σ_b) and "grain boundary" (σ_{gb}) responses at temperatures above 640 K (for the bulk, from *M" vs. freq.* data) or 780 K (for the grain boundary, from *Z" vs. freq.* data) for $Ba_6GaNb_9O_{30}$, and above 740 K for $Ba_6ScNb_9O_{30}$ and $Ba_6InNb_9O_{30}$, was possible to be evaluate.

The electrical conductivity data, σ (where σ=1/*R*), of both bulk and grain boundary components for all three analogues of $Ba_6MNb_9O_{30}$, followed the Arrhenius-type behaviour (Figures 9 and 10) as described by equation 7:

$$\sigma = \sigma_0 \cdot e^{-\left(\frac{E_a}{kT}\right)} \quad (7)$$

where σ_0 is the pre-exponential factor, E_a is the activation energy of the electrical conduction process, k is the Boltzmann constant (1.38×10^{-23} J·K^{-1} or 8.617×10^{-5} eV·K^{-1}) and T is the absolute temperature.

Bulk electrical conductivity, σ_b, evaluated from the $M"_{max}$ *vs. freq.* data contains a systematic error as first a perfect Debye response is assumed in order to calculate C_b using (equation 6). This approximation is further transformed into R_b (from eq. 4, and is equal to $1/(2\pi f_{max}C_b)$), and only used to calculate σ_b. The straight lines of logσ *vs.* (1/*T*) for the bulk electrical conduction in $Ba_6GaNb_9O_{30}$, $Ba_6ScNb_9O_{30}$ and $Ba_6InNb_9O_{30}$ are not parallel (Figure 9); the slopes give different activation energies, but without following a systematic evolution when changing the M^{3+} atom in $Ba_6MNb_9O_{30}$ formula (Table 2).

In the case of the "grain boundary" electrical conductivity, σ_{gb}, evaluated from the $Z"_{max}$ *vs. freq.* data, there is again a simplification of assuming a Debye response in order to

calculate R_b, (equation 5). The straight lines of logσ *vs.* (1/*T*) for $Ba_6GaNb_9O_{30}$, $Ba_6InNb_9O_{30}$ are fairly parallel, while the $Ba_6ScNb_9O_{30}$ one is not (Figure 10). The activation energies for the grain boundary electrical conduction processes, when using the electrical conduction data, are presented in Table 2. The slopes give close activation energies for the Ga and In analogues (0.70 eV, respectively 0.82 eV), while for the Sc analogue the value is larger: 1.127 eV. If relating to the microstructural results, only for the Sc analogue the grains arrangement would have predicted such influence (Figure 4), while for the Ga and In analogues, the influence of the bulk is present and consists in mixing with the "grain boundary" response and therefore lowering the activation energies.

However, in both cases, from the activation energy values it is evident that for the $Ba_6GaNb_9O_{30}$ and $Ba_6InNb_9O_{30}$ pellets, the conduction mechanisms are dominated by the bulk response, while for $Ba_6ScNb_9O_{30}$ pellet the "grain boundary" effects have significant influence.

Figure 9 Arrhenius plot of the bulk electrical conductivity data (from M''_{max} *vs. freq.*) for $Ba_6GaNb_9O_{30}$, $Ba_6ScNb_9O_{30}$ and $Ba_6InNb_9O_{30}$ analogues.

Figure 10 Arrhenius plot of the grain boundary electrical conductivity data (from Z''_{max} *vs. freq.*) for $Ba_6GaNb_9O_{30}$, $Ba_6ScNb_9O_{30}$ and $Ba_6InNb_9O_{30}$ analogues.

Much simpler and direct evaluation may be however performed; the time constants, τ, are directly measured (actually the frequency at the *M"* and *Z"* peak maxima, f_{max}, and τ equals $2\pi f_{max}$) and are more accurate, requiring no additional approximations. It was possible to measure the time constant (τ) of both bulk (τ_b) and "grain boundary" (τ_{gb}) components, at temperatures >640 K (for the bulk, from *M" vs. freq*. data) or 780 K (for the grain boundary, from *Z" vs. freq*. data) for $Ba_6GaNb_9O_{30}$, and above 740 K for Sc and In analogues.

The time constant data, τ (where $\tau = 2\pi f_{max}$), of both bulk and grain boundary components for all three insulating analogues of $Ba_6MNb_9O_{30}$, follow the Arrhenius-type behaviour also (Figure 11), as described by equation 8:

$$\tau = \tau_0 \cdot e^{-\left(\frac{E_a}{kT}\right)} \quad (8)$$

where τ_0 is the pre-exponential factor, E_a is the activation energy of the electrical conduction process, k is the Boltzmann constant (1.38×10^{-23} $J\cdot K^{-1}$ or 8.617×10^{-5} $eV\cdot K^{-1}$) and T is the absolute temperature.

The straight lines $\log\tau$ *vs.* $(1/T)$ for the grain boundary component of all three analogue compounds are parallel (Figure 11) – blue fitting straight lines. The slopes give very close activation energies for all three analogues of $Ba_6ScNb_9O_{30}$, ~ 1.25 eV (Table 2). For $Ba_6ScNb_9O_{30}$ and $Ba_6InNb_9O_{30}$, the *Z"* Debye-like curves (Figures 7a and 8a) do not only evolve in the same manner (characterized by the same activation energies), but they have identical time constants for each investigated temperature (overlapping straight lines and same intercept (τ_0), the pre-exponential factor). Thus, for all three compounds the conduction mechanism of the "grain boundaries" appears to be quite similar.

The fact that the time constant for bulk and "grain boundary" in all three samples is less than an order of magnitude (much less in the case of the Sc and In analogues) and have a similar magnitude of associated capacitance may strongly suggest that they represent the same relaxation process or distribution of relaxation processes.

The resulting activation energies corresponding to the bulk are lower than those of "grain boundaries" (Table 2); for the Sc analogue, however, the bulk activation energy is much higher and more similar to the "grain boundary" one. This is because of the "grain boundary" influence in this particular case, which is mixed with/or also represents the bulk.

The straight lines of $\log\tau$ *vs.* $(1/T)$ for $Ba_6GaNb_9O_{30}$, $Ba_6InNb_9O_{30}$ are fairly parallel, while the $Ba_6ScNb_9O_{30}$ one is not (Figure 11) – green fitting straight lines. The slopes give close activation energies for the Ga and In analogues (0.91 eV, respectively 0.80 eV), while for the Sc analogue the value is larger: 1.23 eV and as described in the precedent paragraph, it is the same as for the "grain boundary" one.

Figure 11 Arrhenius plots of the bulk and grain boundary time constant data (from $M"_{max}$ *vs. freq.* and respectively from $Z"_{max}$ *vs. freq.*) for $Ba_6GaNb_9O_{30}$, $Ba_6ScNb_9O_{30}$ and $Ba_6InNb_9O_{30}$ analogues.

If comparing the results obtained by using the electrical conductivity (σ) data to those obtained by using the time constant (τ) data, it becomes evident that the last ones are more reliable. This is because the time constant is a measured quantity, while the electrical conductivity is a quantity that requires assumptions and some mathematical calculations when processing the experimental data.

Table 2 Activation energies for the bulk and "grain boundary" of $Ba_6M^{3+}Nb_9O_{30}$ electrical conduction processes; data extracted from the electrical conductivity, σ, and time constant, τ.

where "*r*" is the correlation coefficient.

Generally, the "grain boundary" activation energy (in average) of the electrical conduction process ($\bar{E}_a$ = 1.25 eV) is higher with 0.40 eV than the bulk activation energy (in average) of the electrical conduction process ($\bar{E}_a$ = 0.85 eV). The conduction mechanisms are dominated by the bulk response, the samples all being insulators.

4. Conclusions

A family of relaxor dielectrics with the tetragonal tungsten bronze structure (nominal composition $Ba_6M^{3+}Nb_9O_{30}$, M^{3+} = Ga, Sc or In) was studied using scanning electron microscopy for characterising the pellet microstructure and by high temperature impedance spectroscopy to identify the electroactive regions within these materials by calculating the capacitances and the resistances of both grain boundaries and bulk parts. The electric conductivities and the time constants were determined, while the contribution of the bulk and grain boundaries to the electrical conduction processes were understood.

For the Ga and In analogues, the SEM images of the pellets have revealed good, dense internal microstructures, with well-bonded grains and only discrete porosity; the majority of the grains have almost completely fused into big lumps of material with irregular shape and formed continuous interfaces. However, the Sc analogue pellet does not have a very good internal microstructure, with many small and poorly-bonded grains, gathered in agglomerates (linked by some independent small grains with irregular shapes and dimensions) and also with independent small grains exceeding and randomly distributed, resulting in significant continuous porosity and poorly defined grain boundary regions. They have revealed broadly similar electric behaviour of the three compounds: electrical insulators, with only moderate level of conductivity at temperatures above 623 K (350 °C). In the Sc analogue case, the time constants (τ) of both bulk (τ_b) and grain boundary (τ_{gb}) components have almost the same values, this fact relating to the poor microsctructure of the pellet as was evidenced previously (the shape, volume and arrangement of ceramic grains were expected to give a greater contribution for the grain boundaries to the overall process). From the activation energy values of the electrical conduction process it was evident that for $Ba_6GaNb_9O_{30}$ and $Ba_6InNb_9O_{30}$ the conduction mechanisms are dominated by the bulk response, while for

$Ba_6ScNb_9O_{30}$ the grain boundary effects mix strongly with the bulk response making it hard to clearly assign a specific grain boundary contribution.

Acknowledgements: The authors would like to thank to the following funding organisations: the Royal Society for providing a research fellowship (F.D.M.), EPSRC for providing the PhD student grant (A.R.) and Roberto Rocca Education Program for providing an additional fellowship (A.R.).

References

[1] Tilley, R. *Understanding Solids: The Science of Materials*, John Wiley and Sons - VCH, **2004**.

[2] Lines, M.E.; Glass, A.M. *Principles and applications of ferroelectrics and related materials*, Oxford University Press, **2001**.

[3] Shrout, T.R.; Zhang, S.J. Lead-free piezoelectric ceramics: Alternatives for PZT?. *J. Electroceram.*, **2007**, 19, 111-124.

[4] Wilk, G.D.; Wallace, R.M.; Anthony, J.M. High-κ gate dielectrics: Current status and materials properties considerations. *J. Appl. Phys.* **2001**, 89, 5243-5275

[5] Cross, L.E. *Ferroelectric ceramics: tailoring properties for specific applications*, Ferroelectric Ceramics, Ed.: N. Setter and E.L. Colla, Basel, Birkhauser, **1993**.

[6] Pithan, C.; Hennings D.; Waser, R. Progress in the synthesis of nanocrystalline $BaTiO_3$ powders for MLCC. *Int. J. Appl. Ceram. Technol.* **2005**, 2, 1-14.

[7] Sakabe, Y. ; Multilayer ceramic capacitors. *Curr. Opin. Solid State Mater. Sci.* **1997**, 2, 584-587.

[8] Jayalakshmi, M.; Balasubramanian, K.; Simple capacitors to supercapacitors-an overview. *Int. J. Electrochem. Sci.* **2008**, 3, 1196.

[9] Damjanovic, D. Ferroelectric, dielectric and piezoelectric properties of ferroelectric thin films and ceramics. *Rep. Prog. Phys.*, **1998**, 61, 1267.

[10] Hirota, K.; Wakimoto, S.; Cox, D.E. Neutron and x-ray scattering studies of relaxors. *J. Phys. Soc. Jpn.* **2006**, 75, 111006.

[11] Jeong, D.Y. *PhD Thesis*, The Pennsylvania State University, **2004**.

[12] Shvartsman, V.V.; Lupascu, D.C. Lead-Free Relaxor Ferroelectrics. *J. Am. Ceram. Soc.* **2012**, 95, 1-26.

[13] Rotaru, A. *PhD Thesis*, University of St Andrews, **2013**.

[14] Villafuerte-Castrejon, M.E.; Moran, E.; Reyes-Montero, A.; Vivar-Ocampo, R.; Pena-Jimenez, J-.A.; Rea-Lopez, S.-O.; Pardo, L. Towards Lead-Free Piezoceramics: Facing a Synthesis Challenge. *Materials* **2015**, 9, 21.

[15] Zu, X.; Fu, M.; Stennett, M.C.; Villarinho, P.M.; Levin, I.; Randall, C.A.; Gardner, J.; Morrison, F.D.; Reaney, I.M. A Crystal-Chemical Framework for Relaxor versus Normal Ferroelectric Behavior in Tetragonal Tungsten Bronzes. *Chem. Matter.* **2015**, 27, 3250–3261.

[16] Arnold, D.C.; Morrison, F.D. B-cation effects in relaxor and ferroelectric tetragonal tungsten bronzes. *J. Mater. Chem.* **2009**, 19, 6485-6488.

[17] Rotaru, A.; Miller, A.J.; Arnold, D.C.; Morrison, F.D. Towards novel multiferroic & magnetoelectric materials: dipole stability in tetragonal tungsten bronzes. *Phil. Trans. Royal Soc. A: Math. Phys. Eng. Sci.* **2014**, 372, 20120451.

[18] Gardner, J.; Morrison, F.D. A-site size effect in a family of unfilled ferroelectric tetragonal tungsten bronzes: $Ba_4R_{0.67}Nb_{10}O_{30}$ (R = La, Nd, Sm, Gd, Dy and Y). *Dalton Trans.* **2014**, 43, 11687-11695.

[19] Qu, W.; Tan, X.; McCallum, R.W.; Cann, D.P.; Ustundag, E. Room temperature magnetoelectric multiferroism through cation ordering in complex perovskite solid solutions. *J. Phys.: Cond. Matter* **2006**, 18, 8935.

[20] Simon, A.; Ravez, J. Solid-state chemistry and non-linear properties of tetragonal tungsten bronzes materials. *C. R. Chimie*, **2006**, 9, 1268-1276.

[21] Stennett, M.C.; Miles, G.C.; Sharman, J.; Reaney, I.M.; West, A.R. A new family of ferroelectric tetragonal tungsten bronze phases, $Ba_2MTi_2X_3O_{15}$. *J. Eur. Ceram. Soc.* **2005**, 25, 2471-2475.

[22] Stennett, M.C.; Reaney, I.M.; Miles, G.C.; Woodward, D.I.; West, A.R.; Kirk, C.A.; Levin, I. Dielectric and structural studies of $Ba_2MTi_2Nb_3O_{15}$ ($BMTNO_{15}$, M= Bi^{3+}, La^{3+}, Nd^{3+}, Sm^{3+}, Gd^{3+}) tetragonal tungsten bronze-structured ceramics. *J. Appl. Phys.* **2007**, 101, 4114.

[23] Chen, X.M.; Yang, J.S. Dielectric characteristics of ceramics in $BaO–Nd_2O_3–TiO_2–Ta_2O_5$ system. *J. Eur. Ceram. Soc.* **1999**, 19, 139-142.

[24] Chen, X.M.; Liu, C.L.; Yang, J.S.; Wu, Y.J. Some Tungsten–Bronze Compounds in the $BaO–Nd_2O_3–TiO_2–Ta_2O_5$ System. *J. Solid State Chem.* **1999**, 148, 438-441.

[25] P.R.; Irvine, J.T.S. Synthesis and electrical characterisation of the tetragonal tungsten bronze type phases,$(Ba/Sr/Ca/La)_{0.6}M_xNb_{1-x}O_{3-\delta}$ (M= Mg, Ni, Mn, Cr, Fe, In, Sn): evaluation as potential anode materials for solid oxide fuel cells. *Solid State Ionics* **1999**, 124, 61-72.

[26] Miller, A.J.; Rotaru, A.; Arnold, D.C.; Morrison F.D. Effect of local A-strain on dipole stability in $A_6GaNb_9O_{30}$ (A = Ba, Sr, Ca) tetragonal tungsten bronze relaxor dielectrics. *Dalton Trans.* **2015**, 44, 10738-10745.

[27] Castel E.; Josse, M.; Michau, D.; Maglione, M. Flexible relaxor materials: $Ba_2Pr_xNd_{1-x}FeNb_4O_{15}$ tetragonal tungsten bronze solid solution. *J Phys: Condens Matter.* **2009**, 21, 452201.

[28] Josse, M.; Bidault, O.; Roulland, F.; Castel, E.; Simon, A.; Michau, D.; Von der Muhll, R.; Nguyen, O.; Maglione, M. The $Ba_2LnFeNb_4O_{15}$"tetragonal tungsten bronze": Towards RT composite multiferroics. *Solid State Sci.* **2009**, 11,1118-11123.

[29] Castel, E.; Josse, M.; Roulland, F.; Michau, D.; Raison, L.; Maglione, M. In-situ formation of barium ferrite in iron-doped "tetragonal tungsten bronze": Elaboration of room temperature multiferroic composites. *J. Magn. Magn. Mater.* **2009**, 321, 1773-1777.

[30] Albino, M.; Veber, P.; Pechev, S.; Labrugere, C.; Velazquez, M.; Maglione, M.; Josse, M. Growth and Characterization of $Ba_2LnFeNb_4O_{15}$ (Ln = Pr, Nd, Sm, Eu) Relaxor Single Crystals. *Cryst Growth Design.* **2014**, 14, 500-12.

[31] Roulland, F.; Josse, M.; Castel, E.; Maglione, M. Influence of ceramic process and Eu content on the composite multiferroic properties of the $Ba_{6-2x}Ln_{2x}Fe_{1+x}Nb_{9-x}O_{30}$ TTB system, *Solid State Sci.* **2009**, 11, 1709–1716.

[32] McCabe, E.E.; West, A.R. New high permittivity tetragonal tungsten bronze dielectrics $Ba_2LaMNb_4O_{15}$: M=Mn, Fe. *J. Solid State Chem.* **2010**, 183, 624–630.

[33] Brandt, R.; Muller-Buschbaum, H. Zur Kristallchemie der tetragonalen Wolframbronze: $Ba_6FeNb_9O_{30}$. *Monats. Chem.* **1986**, 117, 1239-1244.

[34] Henshaw, G.S.; Gellman, L.J.; Williams, D.E. Selectivity and composition dependence of response of gas-sensitive resistors. Part 1.—Propane–carbon monoxide selectivity of $Ba_6Fe_xNb_{10-x}O_{30}$ ($1 \leqslant x \leqslant 2$). *J. Mater. Chem.* **1994**, 4, 1427-1431.

[35] Krainik, N.N.; Isupov, V.A.; Bryzhina, M.F.; Agranovskaya, A.I. Crystal chemistry of ferroelectrics with structural type of tetragonal oxygen tungsten bronze. *Soviet Physics – Crystallography* **1964**, 9, 281.

[36] Fang, P.H.; Roth, R.S.; Johnson, H. Class of nonlinear dielectric materials. *J. Am. Ceram. Soc.* **1960**, 43, 169.

[37] Foster, M.C.; Brown, G.R.; Nielson, R.M.; Abrahams, S.C. $Ba_6CoNb_9O_{30}$ and $Ba_6FeNb_9O_{30}$: Two new tungsten-bronze-type ferroelectrics. Centrosymmetry of $Ba_{5.2}K_{0.8}U_{2.4}Nb_{7.6}O_{30}$ at 300 K. *J. Appl. Crystallogr.* **1997**, 30, 495-501.

[38] Ismailzade, I.; Huseynov, N.G.; Sultanov, G.J.; Hajiyev, E.M. Dielectric mossbauer and magnetic investigations of ferroelectric-magnetics $Sr_6Nb_9FeO_{30}$ and $Ba_6Nb_9FeO_{30}$. *Ferroelectrics* **1976**, 13, 389-391.

[39] Rotaru, A.; Arnold, D.C.; Daoud-Aladine, A.; Morrison, F.D. Origin and stability of the dipolar response in a family of tetragonal tungsten bronze relaxors. *Phys. Rev. B.* **2011**, 83, 184302.

[40] Rotaru, A.; Morrison, F.D. Vogel-Fulcher analysis of relaxor dielectrics with the tetragonal tungsten bronze structure $Ba_6MNb_9O_{30}$ (M = Ga, Sc, In). *J. Therm. Anal. Calorim.* **2015**, 120, 1249-1259.

[41] Rotaru, A.; Schiemer J.A.; Carpenter, M.A. Elastic and anelastic relaxations accompanying relaxor dielectric behaviour of $Ba_6GaNb_9O_{30}$ tetragonal tungsten bronze from resonant ultrasound spectroscopy. *J. Therm. Anal. Calorim.* **2016**, 124, 571-583.

[42] Kimura, T.; Yi, Y.; Sakurai, F. Mechanisms of Texture Development in Lead-Free Piezoelectric Ceramics with Perovskite Structure Made by the Templated Grain Growth Process. *Materials* **2010**, 3, 4965-4978.

[43] Lalena, J.N.; Cleary, D.A. *Principles of Inorganic Materials Design*, John Wiley & Sons Inc., Hoboken, New Jersey, **2005**.

[44] Irvine, J.T.S.; Sinclair, D.C.; West, A.R. Electroceramics: characterization by impedance spectroscopy. *Adv. Mater.* **1990**, 2, 132-138.

[45] Pradhan, D.K.; Behera, B.; Das, P.R. Studies of dielectric and electrical properties of a new type of complex tungsten bronze electroceramics. *J. Mater. Sci.: Mater. Electron.* **2012**, 23, 779–785.

[46] Dimos, D.; Chaudhari, P.; Mannhart J.; LeGoues, F.K. Orientation Dependence of Grain-Boundary Critical Currents in $YBa_2Cu_3O_{7-\delta}$ Bicrystals. *Phys. Rev. Lett.* **1988**, 61, 219.

[47] Ihrig, H.; Klerk, M. Visualization of the grain-boundary potential barriers of PTC-type $BaTiO_3$ ceramics by cathodoluminescence in an electron-probe microanalyzer. *Appl. Phys. Lett.* **1979**, 35, 307-309.

[48] Hirose N.; West, A.R. Impedance spectroscopy of undoped $BaTiO_3$ ceramics. *J. Am. Ceram. Soc.*, **1996**, 79, 1633-1641.

[49] Bruce, P.G.; West, A.R. The A-C Conductivity of Polycrystalline LISICON, $Li_{2+2x}Zn_{1-x}GeO_4$, and a Model for Intergranular Constriction Resistances. *J. Electrochem. Soc.* **1983**, 130, 662-669.

[50] Johnson, D. Scribner Associates, Inc., **1995-2000**.

[51] Egerton, R.F. *Physical Principles of Electron Microscopy – An introduction to TEM, SEM and AEM*, Springer Science+Business Media, LLC, Printed in United States of America, **2007**.

[52] Morrison, F.D.; Sinclair, D.C.; West, A.R. Electrical and structural characteristics of lanthanum-doped barium titanate ceramics. *J. Appl. Phys.* **1999**, 86, 6355-6366.

[53] Pati, B.; Choudhary, C.N.P.; Das, P.R. Studies of dielectric, pyroelectric and conduction mechanism of $Sr_3Ta_2O_8$. *Ceram. Int.* **2014**, 40, 2201–2208.

[54] Bouziane, M.; Taibi, M.; Boukhari, A. Phase transition and conduction mechanism in $Pb_2Na_{0.8}R_{0.2}Nb_{4.8}Fe_{0.2}O_{15}$ material (R= rare earth). *J. Solid State Chem.* **2013**, 207, 203-207.

[55] Hodge, I.M.; Ingram, M.D.; West, A.R. Impedance and modulus spectroscopy of polycrystalline solid electrolytes. *J. Electroanal. Chem.* **1976**, 74, 125-143.

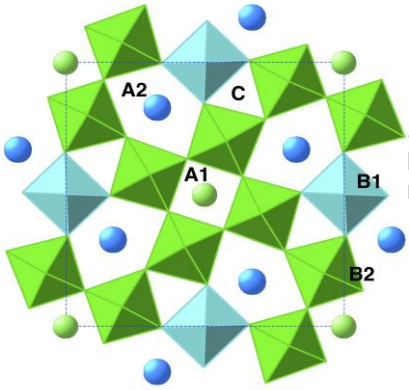

Figure 1 Polyhedral representation of the tetragonal tungsten bronze (TTB) aristotype structure viewed down the c-axis.

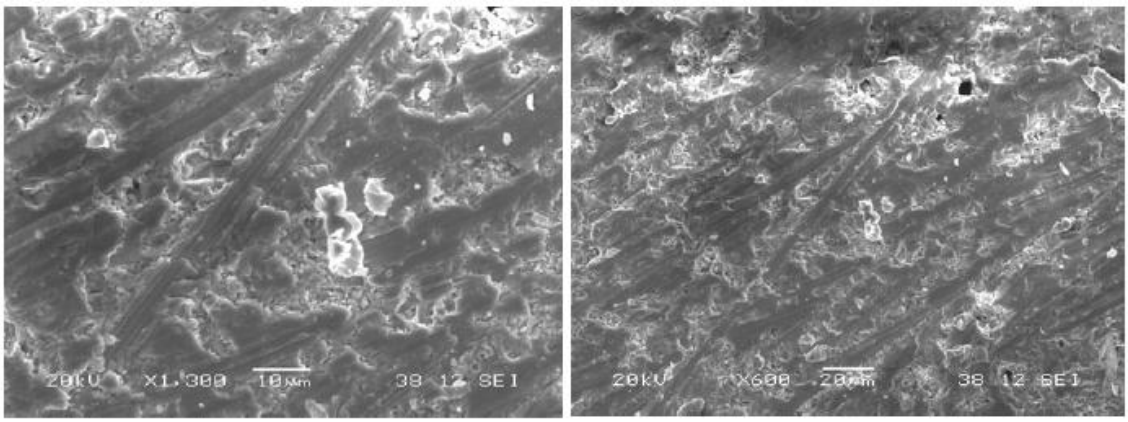

a) b)

Figure 2 SEM micrographs for the external surfaces of a $Ba_6InNb_9O_{30}$ pellet.

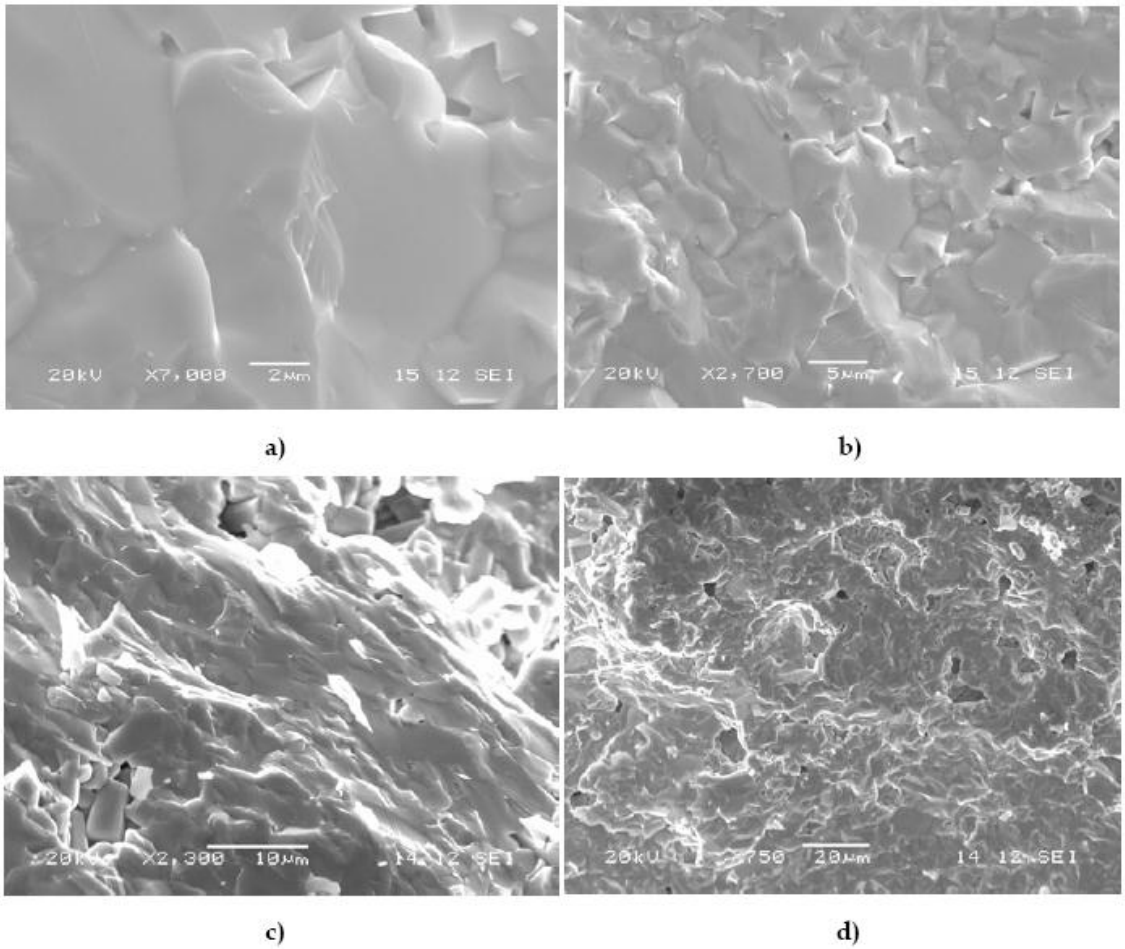

Figure 3 SEM images of the fracture surface of a $Ba_6GaNb_9O_{30}$ pellet sintered at 1300 °C.

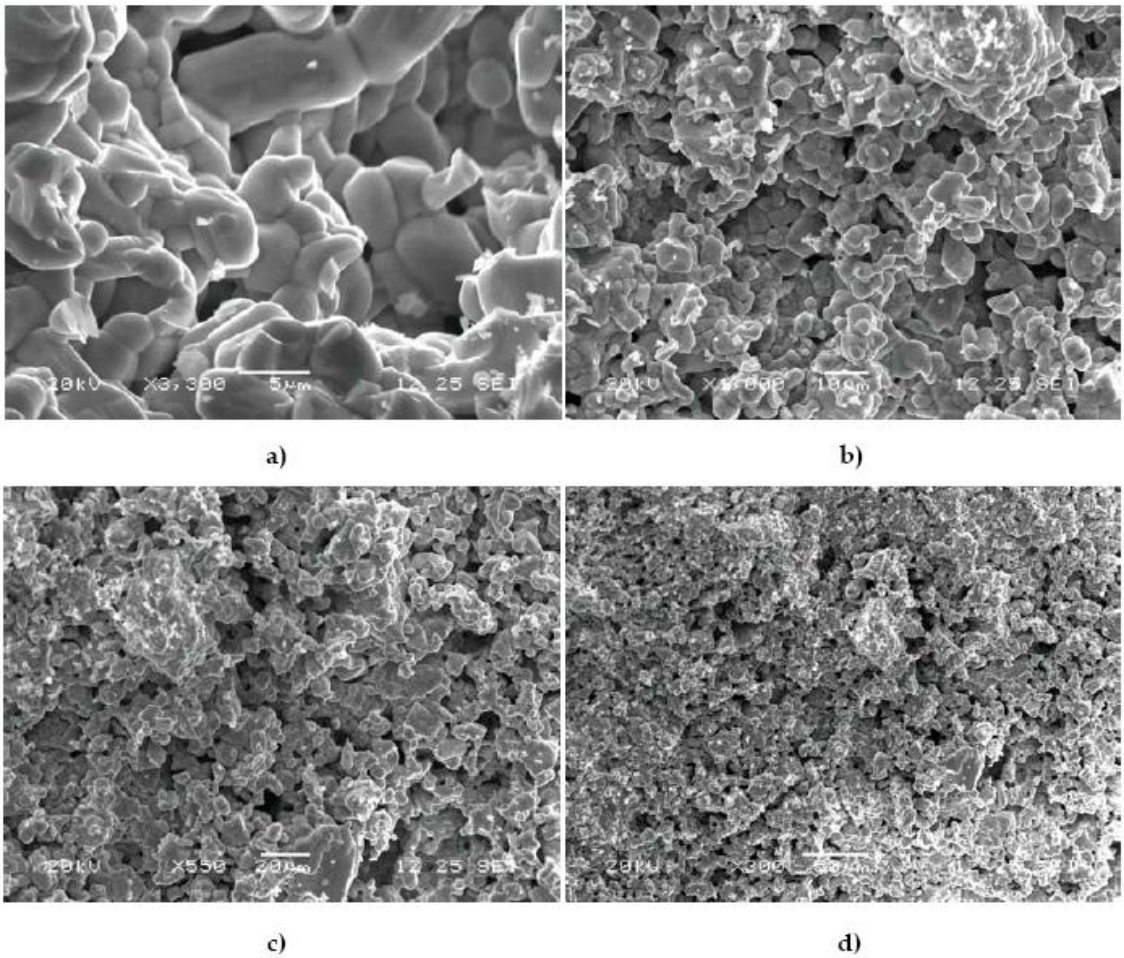

Figure 4 SEM images of the fracture surface of a $Ba_6ScNb_9O_{30}$ pellet obtained at 1350 °C.

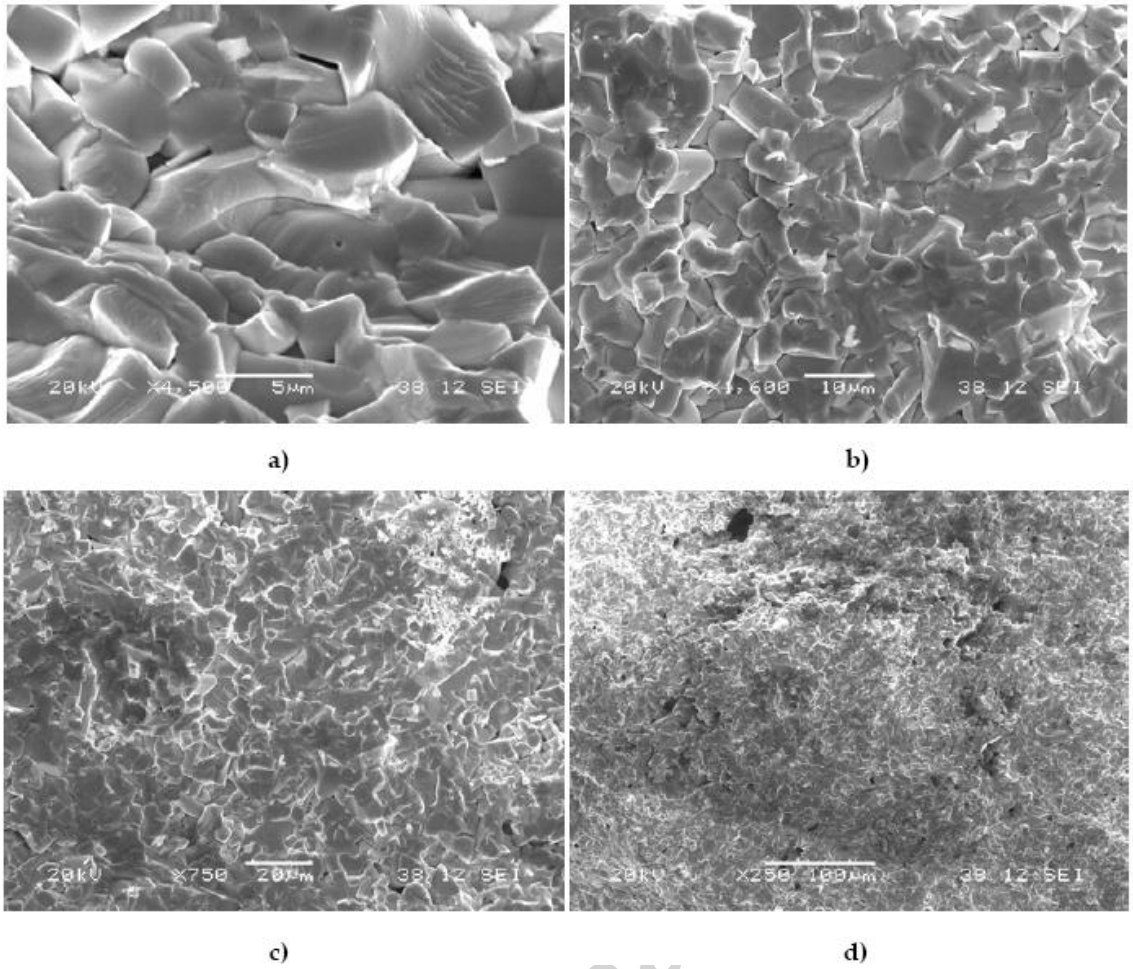

Figure 5 SEM images of the fracture surface of a $Ba_6InNb_9O_{30}$ pellet obtained at 1350 °C.

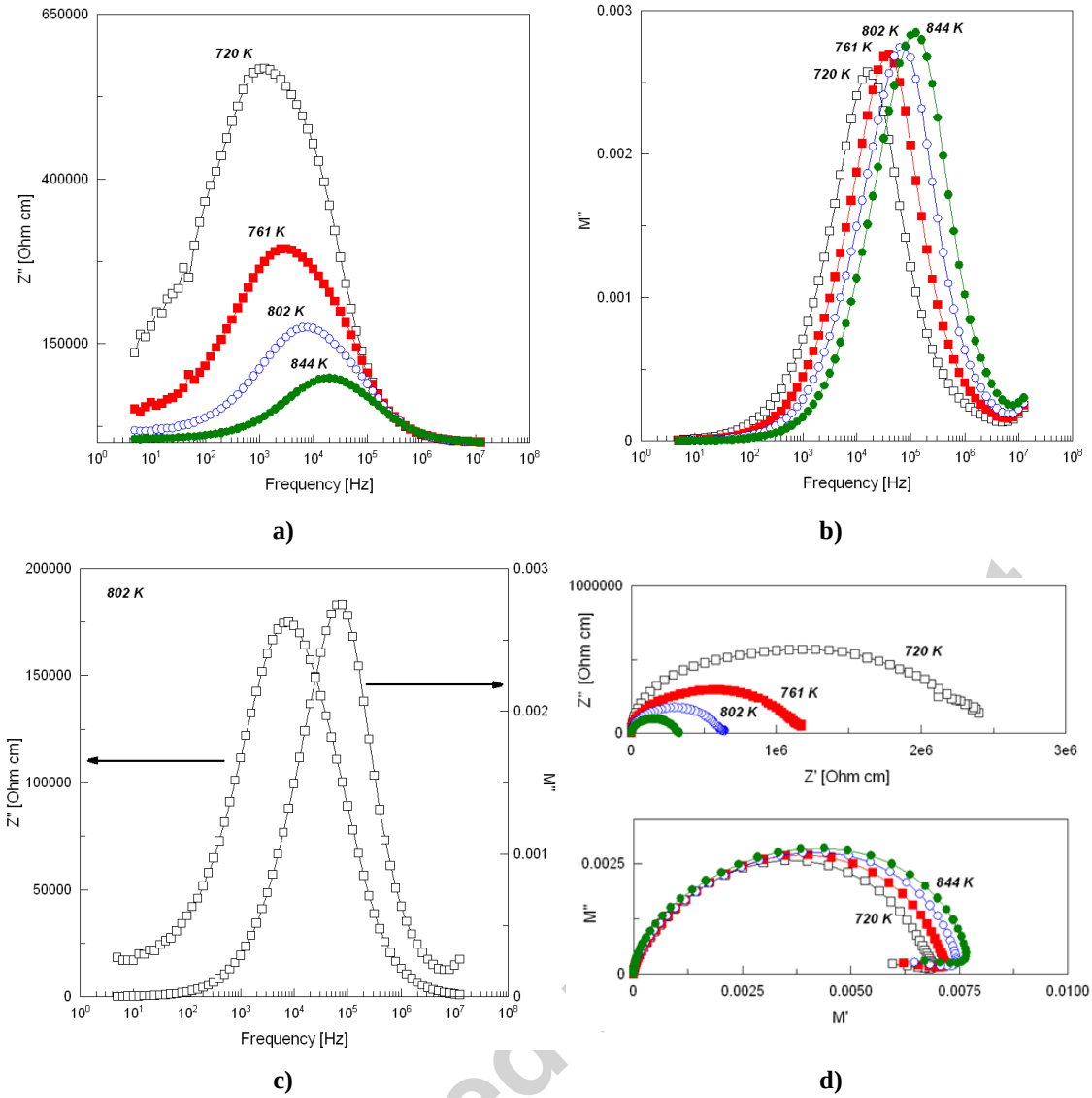

Figure 6 Selective high-temperature impedance spectroscopy data for $Ba_6GaNb_9O_{30}$: spectroscopic plot of *Z''* (a), *M''* (b) and combined *Z''* and *M''* plot at 802 K (c); complex impedance (*Z**) and modulus (*M**) plots (d).

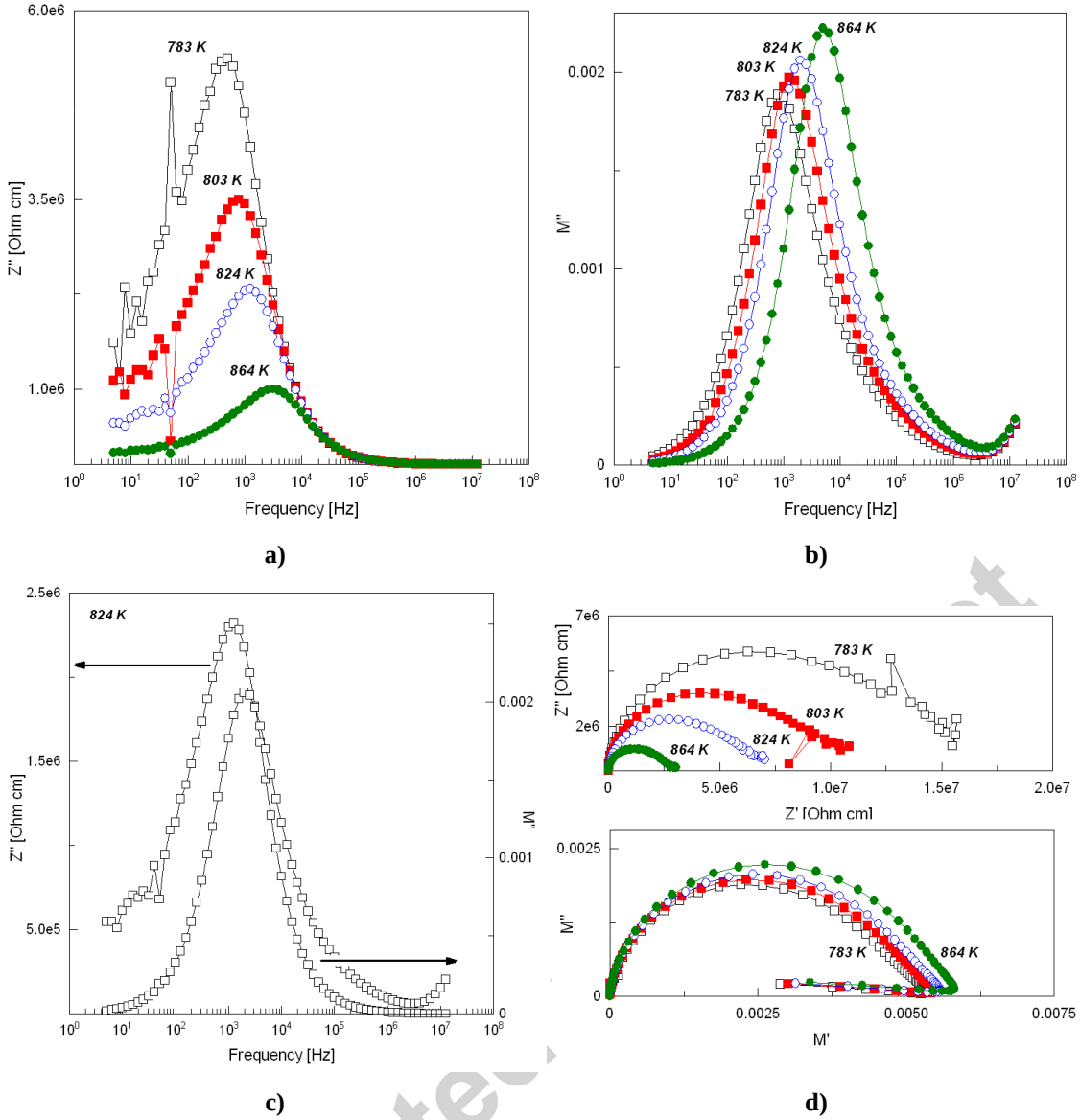

Figure 7 Selective high-temperature impedance spectroscopy data for $Ba_6ScNb_9O_{30}$: spectroscopic plot of *Z''* (a), *M''* (b) and combined *Z''* and *M''* plot at 824 K (c); complex impedance (*Z**) and modulus (*M**) plots (d).

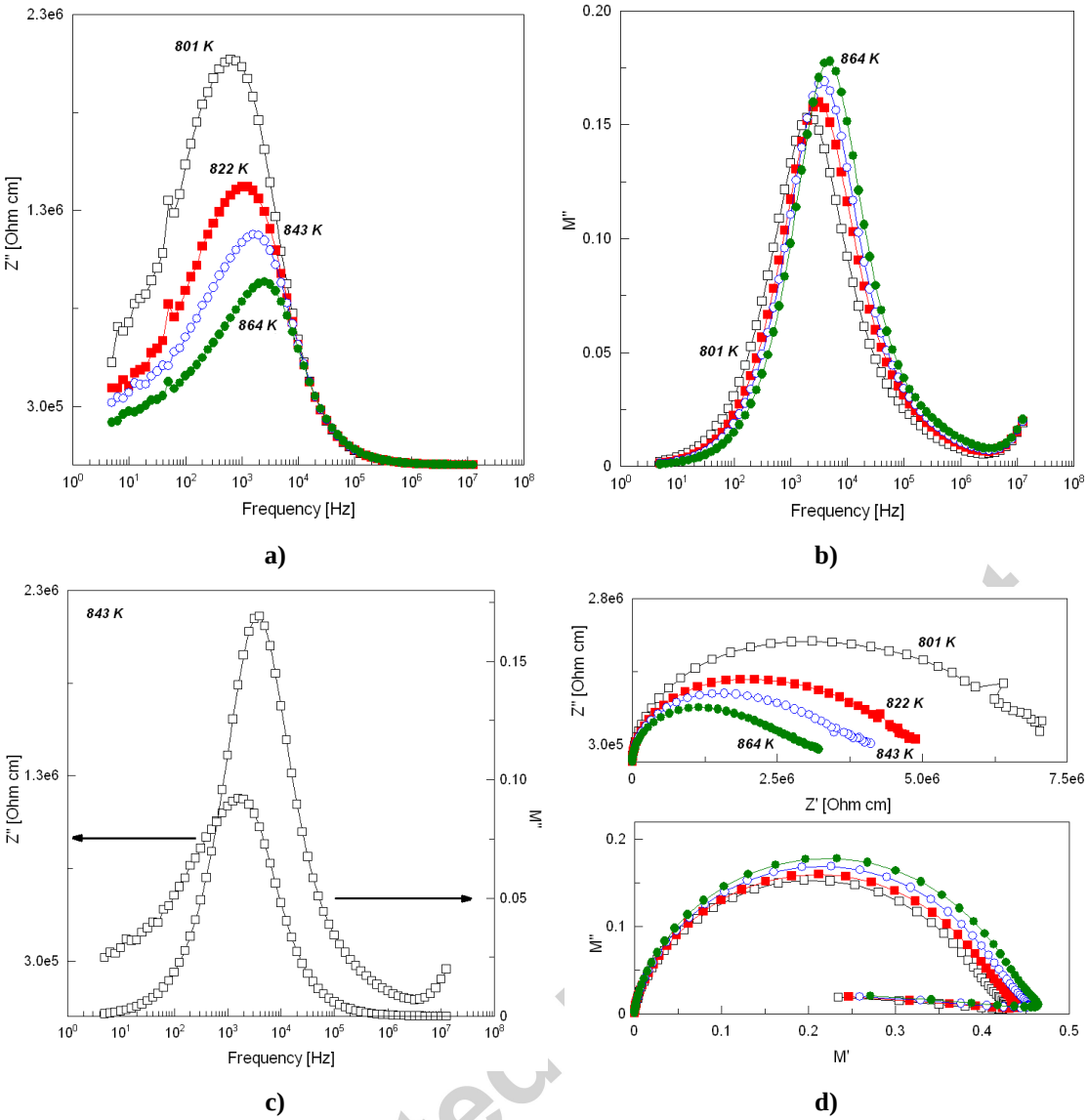

Figure 8 Selective high-temperature impedance spectroscopy data for $Ba_6InNb_9O_{30}$: spectroscopic plot of *Z''* (a), *M''* (b) and combined *Z''* and *M''* plot at 843 K (c); complex impedance (*Z**) and modulus (*M**) plots (d).

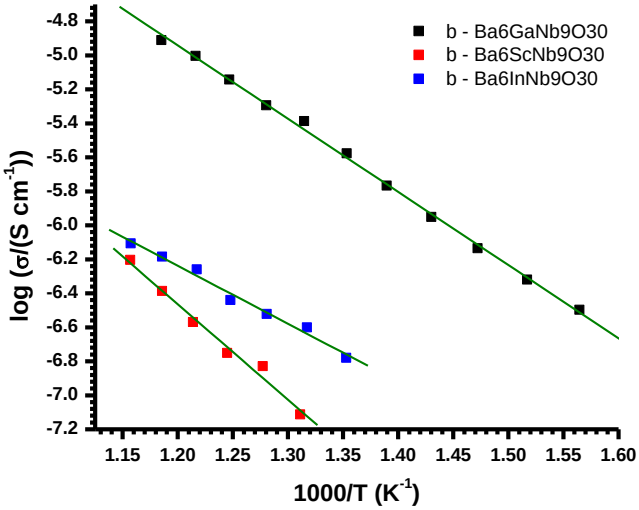

Figure 9 Arrhenius plot of the bulk electrical conductivity data (from M''_{max} *vs. freq.*) for $Ba_6GaNb_9O_{30}$, $Ba_6ScNb_9O_{30}$ and $Ba_6InNb_9O_{30}$ analogues.

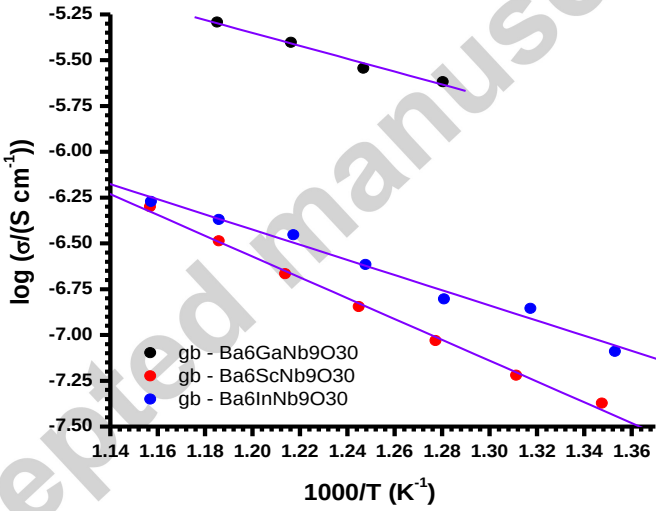

Figure 10 Arrhenius plot of the grain boundary electrical conductivity data (from Z''_{max} *vs. freq.*) for $Ba_6GaNb_9O_{30}$, $Ba_6ScNb_9O_{30}$ and $Ba_6InNb_9O_{30}$ analogues.

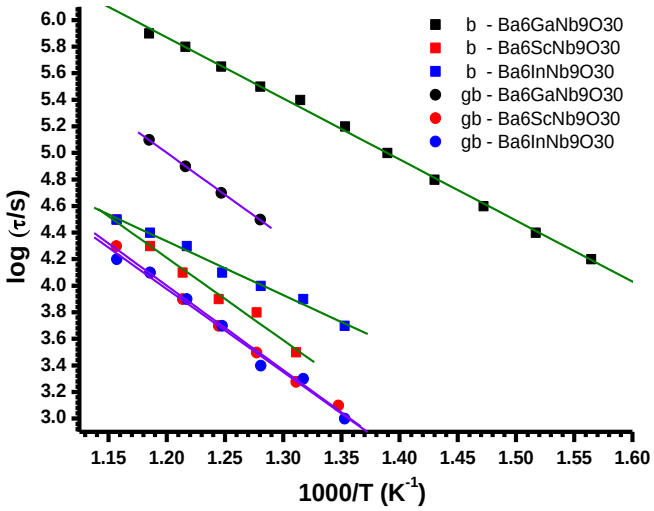

Figure 11 Arrhenius plots of the bulk and grain boundary time constant data (from M''_{max} *vs. freq.* and respectively from Z''_{max} *vs. freq.*) for $Ba_6GaNb_9O_{30}$, $Ba_6ScNb_9O_{30}$ and $Ba_6InNb_9O_{30}$ analogues.

Table 1 Fabrication details of $Ba_6M^{3+}Nb_9O_{30}$ (M^{3+} = Ga^{3+}, Sc^{3+}, In^{3+}) ceramic powders and pellets, and relative densities of the resulting pellets used for electrical studies

Compound	***Reaction temperatures/°C and (Reaction time/h)***	***Sintering temperatures/°C***	***Relative density/%***
$Ba_6GaNb_9O_{30}$	1250 °C (12h) + 1250 °C (12h) +1300 °C (6.5h)	1300 °C (6.5h)	94.55
$Ba_6ScNb_9O_{30}$	1250 °C (12h) + 1250 °C (12h) +1350 °C (6.5h)	1350 °C (6.5h)	88.65
$Ba_6InNb_9O_{30}$	1250 °C (12h) + 1250 °C (12h) +1350 °C (6.5h)	1350 °C (6.5h)	92.15

Table 2 Activation energies for the bulk and "grain boundary" of $Ba_6M^{3+}Nb_9O_{30}$ electrical conduction processes; data extracted from the electrical conductivity, σ, and time constant, τ.

Compound	σ_{bulk} ***(M'' vs. f data)***	"$\sigma_{grain\ boundary}$" ***(Z'' vs. f data)***	τ_{bulk} ***(M'' vs. f data)***	"$\tau_{grain\ boundary}$" ***(Z'' vs. f data)***
$Ba_6GaNb_9O_{30}$	E_a=**0.854**±0.012	E_a=**0.700**±0.066	E_a=**0.912**±0.013	E_a=**1.253**±0.017
	r=0.99907	*r*=0.99104	*r*=0.99900	*r*=0.99980
$Ba_6ScNb_9O_{30}$	E_a=**1.114**±0.083	E_a=**1.127**±0.031	E_a=**1.233**±0.065	E_a=**1.262**±0.028
	r=0.99272	*r*=0.99810	*r*=0.99440	*r*=0.99877
$Ba_6InNb_9O_{30}$	E_a=**0.676**±0.036	E_a=**0.820**±0.047	E_a=**0.803**±0.036	E_a=**1.238**±0.059
	r=0.99287	*r*=0.99181	*r*=0.99498	*r*=0.99435

where "*r*" is the correlation coefficient.